Journal of Biomedical Optics

BiomedicalOptics.SPIEDigitalLibrary.org

# Determination of cell nucleus-to-cytoplasmic ratio using imaging flow cytometry and a combined ultrasound and photoacoustic technique: a comparison study

Michael J. Moore
Joseph A. Sebastian
Michael C. Kolios

SPIE.

Michael J. Moore, Joseph A. Sebastian, Michael C. Kolios, "Determination of cell nucleus-to-cytoplasmic ratio using imaging flow cytometry and a combined ultrasound and photoacoustic technique: a comparison study," *J. Biomed. Opt.* **24**(10), 106502 (2019), doi: 10.1117/1.JBO.24.10.106502.

# Determination of cell nucleus-to-cytoplasmic ratio using imaging flow cytometry and a combined ultrasound and photoacoustic technique: a comparison study

**Michael J. Moore,[a,b,c] Joseph A. Sebastian,[a,b,c] and Michael C. Kolios[a,b,c,*]**
[a]Ryerson University, Department of Physics, Faculty of Science, Toronto, Ontario, Canada
[b]Ryerson University and St. Michael's Hospital, Institute for Biomedical Engineering and Science Technology, Toronto, Ontario, Canada
[c]Li Ka Shing Knowledge Institute, Keenan Research Center for Biomedical Science, St. Michael's Hospital, Toronto, Ontario, Canada

**Abstract.** While the nucleus-to-cytoplasmic (N:C) ratio has traditionally been used for assessing cell malignancy, most N:C measurement techniques are time-consuming and performed on thin histological sections, which prohibit assessment of three-dimensional cell structure. A combined ultrahigh frequency ultrasound (US) and photoacoustic (PA) technique was used to assess the size and N:C ratio of cultured cancer cells in three dimensions (3D). The diameters of the cells and their stained nuclei were obtained by fitting the power spectrum of backscattered US pulses and emitted PA waves, respectively, to well-established theoretical models. For comparison, an imaging flow cytometer (IFC) was also used to determine the two-dimensional cell and nucleus sizes from large cell populations using brightfield and fluorescence images, respectively. An N:C ratio was calculated for each cell using the quotient of the measured nucleus diameter and the total cell diameter. The mean N:C ratios calculated using the sound-based approach were 0.68, 0.66, and 0.54 for MCF-7, PC-3, and MDA-MB-231 cells, respectively, and were in good agreement with the corresponding values of 0.68, 0.67, and 0.68 obtained using the IFC. The combined US and PA technique, which assesses cellular N:C ratio in 3D, has potential applications in the detection of circulating tumor cells in liquid biopsies.  [DOI: 10.1117/1.JBO.24.10.106502]

Keywords: ultrahigh frequency; biological cell; nucleus-to-cytoplasmic; cell sizing; nucleus sizing.

Paper 190258R received Jul. 20, 2019; accepted for publication Sep. 9, 2019; published online Oct. 17, 2019.

## 1 Introduction

The development of new techniques and methods for cancer diagnosis is an active area of scientific and clinical research. Currently, the most commonly used technique for cancer diagnosis is histological assessment of tissue samples excised from the potentially cancerous tissue via optical microscopy.[1] Albeit the gold standard, histological assessment of tissue samples via optical microscopy is a time-consuming and low-throughput process that lacks the ability to adequately assess three-dimensional (3-D) cell structure, a critical component of accurate diagnostics.[2] One of the most prevalent characteristics of cancerous cells is an enlarged nucleus due to the increased amounts of chromatin present within malignant cells. This hallmark of malignancy led to the development of the nucleus-to-cytoplasmic (N:C) ratio, defined as the ratio of the cross-sectional area of the nucleus divided by that of cytoplasm, which has since become a commonly used parameter in tumor staging and grading.[3] Most N:C assessment techniques are typically performed in two dimensional (2-D) thinly sliced histological sections; hence, they may not accurately represent the true 3-D cell structure and may not accurately represent the N:C ratio of the cells being examined. Furthermore, it has been well reported that interobserver variability exists between pathologists using optical microscopy images to calculate the N:C ratio.[4–6]

These shortcomings have led to the development of alternative systems for N:C ratio quantification. Emerging technologies such as digital image analysis using HALO imaging-analysis software in urine cytology,[7] immunofluorescence microscopy paired with ImageJ,[8] and 3-D multiphoton microscopy[9] have been used to assess the N:C ratio but all require a lengthy imaging/analysis time for individual cells. Flow cytometry (FC) overcomes the drawback of slow analysis speeds at the expense of direct measurements of cell morphology. FC can quantitatively assess large cell populations using signals from emitted fluorescence as well as transmitted and scattered light from each cell with speed, automation, and objectivity.[10] Although conventional FC is superior to optical microscopy in its speed and automation, it lacks the ability to generate absolute values for cell or nucleus size.[11] Recent cytometric advances have seen the development of a new modality, imaging flow cytometry (IFC), which combines conventional light microscopy with high-quality CCD cameras in the context of a conventional FC system to image single cells in suspension at high resolution.[11–13] Imaging of single cells in suspension is advantageous as it mimics biological cells in flow, such as those that would be found in the blood.[14,15] IFC analysis software provides analytic tools that utilize feature-based image-gating strategies to characterize cell size, shape, and intensity patterns.[16] IFC incorporates the high-quality image resolution and morphological content of optical microscopy while maintaining the high-throughput, automation, and population statistics of conventional FC.[17] In previous studies, IFC has been used to generate images of single cells

*Address all correspondence to Michael C. Kolios, E-mail: mkolios@ryerson.ca

[e.g., red blood cells (RBCs),[15] platelets[18]] as well as organelles (e.g., nuclei,[19] cytoplasm[20]). However, although IFC analyzes larger cell populations, these measurements are still limited to 2D only. Therefore, there is still an unmet need for an approach that can perform similar analysis while simultaneously ascertaining the 3-D structure of single cells and their organelles, as would be ideal for N:C ratio characterization.

Photoacoustic (PA) imaging is a hybrid modality based on the PA effect[21] that has generated much interest due to its ability to image vasculature without the need for exogenous contrast agents,[22] as well as biological processes involving neural dynamics[23] and myelin distribution.[24] In the PA effect, a sample is irradiated with short (typically nanosecond) laser pulses, inducing a thermoelastic expansion of the light-absorbing chromophores, which in turn generate pressure waves that can then be detected using ultrasound (US) transducers.[21] These recorded PA waves can subsequently be used to generate images that reflect the spatial distribution of optical absorbers within the sample.[25] Alternatively, signal analysis techniques can be applied to individually acquired PA radio-frequency (RF) lines to ascertain information pertaining to the morphology of the source object.[26] When applied to PA signals containing ultrahigh frequencies (UHFs), such techniques enable the extraction of 3-D morphological information of optically absorbing cells such as RBCs and melanocytes.[27–29] Combining PA spectral analysis techniques with an equivalent US-based technique, capable of determining the size of liquid droplets from features in the power spectrum of backscattered US waves,[30,31] we have previously been able to assess the N:C ratio in cultured cancer cells.[32,33] However, our previous work only demonstrated the use of these techniques for a single cell line with a small sample size and used published N:C ratio values as a preliminary means of technique validation. Here, we present an improved spectral analysis technique for the 3-D assessment of the N:C ratio and compare the results of our technique to 2-D IFC measurements of cell populations from the same cell lines.

## 2 Methods

### 2.1 *Cell Preparation*

Cells used for experimentation were prepared as follows: (1) MCF-7 and MDA-MB-231 cells were cultured in Dulbecco's modified Eagle medium (Sigma-Aldrich) containing 10% fetal bovine serum by volume and (2) PC-3 cells were cultured in Roswell Park Memorial Institute medium (Sigma-Aldrich) containing 10% fetal bovine serum by volume. Once confluent, cells were trypsinized and resuspended in phosphate-buffered saline (PBS). The cells were then incubated in a dark room at room temperature for 15 min with a 1:200 solution of DRAQ-5 (Thermo Fisher), a fluorescent nuclear dye. DRAQ-5 staining enabled the production of both fluorescence and PA signals from the cell nucleus. After staining, all cells were washed three times in PBS. The final cell pellet was resuspended in 200 $\mu$l of PBS and was aspirated and expelled into the reservoir of a 25-gauge needle several times to form a single-cell suspension. To prepare the sample for analysis with the US/PA technique, 2 $\mu$l of the cell suspension was added to an aliquot containing 18 $\mu$l of molten 0.5% (w/v) agarose in PBS at 40°C. At these low concentrations, agarose has acoustic properties similar to that of water and, once solidified, gently immobilizes the cells in a spherical shape for the duration of the measurement procedure. A thin layer of cell-containing molten agarose was pipetted onto a glass-bottomed Petri dish (MatTek), which had previously been coated with a layer of 0.5% agarose. Prior to measurement, the dish was left to solidify at room temperature for 30 min. The remainder of the single-cell solution was transferred to a 1.5-ml low-retention microfuge tube to be used for the IFC experiments.

### 2.2 *Image Flow Cytometer Cell Measurement and Image Processing*

An Amnis ImageStreamX® MarkII IFC (MilliporeSigma) equipped with a 5-laser 12-channel system was used for image acquisition. The channels on the IFC correspond to spectral imaging bands. In this study, channels 1 (420 to 480 nm), 9 (570 to 595 nm), and 11 (660 to 740 nm) were used for acquisition along with a 642-nm laser (150 mW). Cell image analysis was carried out using the Amnis IDEAS® software platform (version 6.2). The nucleus diameter and cell diameter were determined using a custom workflow in IDEAS, which is illustrated in Fig. 1(a). As shown in Fig. 1(a) plot I, the gradient root-mean-squared feature was applied to the acquired MCF-7, PC-3, and MDA-MB-231 images, and the corresponding values were plotted on a normalized relative frequency distribution to discriminate between unfocused (low gradient) and focused (high gradient) cell images. Plot II depicts the area and aspect ratio features combined to discriminate between images containing single cells [green region of interest (ROI)] from those containing multiple cells. In our workflow, we included cell images with an aspect ratio between 0.6 and 1 to avoid cell fragments and other debris. Plot III shows the raw centroid X feature, defined as the number of pixels in the horizontal axis from the upper left corner of the image to the center of the mask, plotted against a normalized relative frequency distribution to remove clipped cell images. Lastly, plot IV depicts a positive gate for DRAQ-5-positive cells that was obtained using fluorescence intensity and area features. Through gating for solely DRAQ-5-positive cells in plot IV, we exclude cell images containing calibration beads, which are required for alignment of the sample stream during imaging. Figure 1(b) shows the masks used for the image analysis process. Eroded masks were applied to the final cell population to enable an accurate measurement of the cell diameter (i.e., the diameter of the circle with the same area of the masked object) using the native diameter function in IDEAS. This function was also applied to the masked nucleus image to assess the diameter of the cell nucleus.

### 2.3 *Ultrasound/Photoacoustic Cell Measurement and Signal Processing*

The US and PA measurements were performed using a dual modality UHF PA microscope (Kibero GmbH, Germany). The system consists of an inverted Olympus IX81 optical microscope equipped with a 10× objective (Olympus, Japan). The microscope was modified to incorporate a pulsed 532-nm laser with a 330-ps pulse width and 4-kHz repetition rate (Teem Photonics Inc., France), and a UHF single-element transducer with a central frequency of 375 MHz and a −6 dB bandwidth of 150 MHz. The transducer and objective were aligned such that their focal zones overlapped one another. Pulse-echo US was used to insonify the cells, and laser irradiation of the sample induced a PA wave originating from the cell nucleus. The 375-MHz US transducer was used to record both the backscattered US and the emitted PA signals from the cell and nucleus,

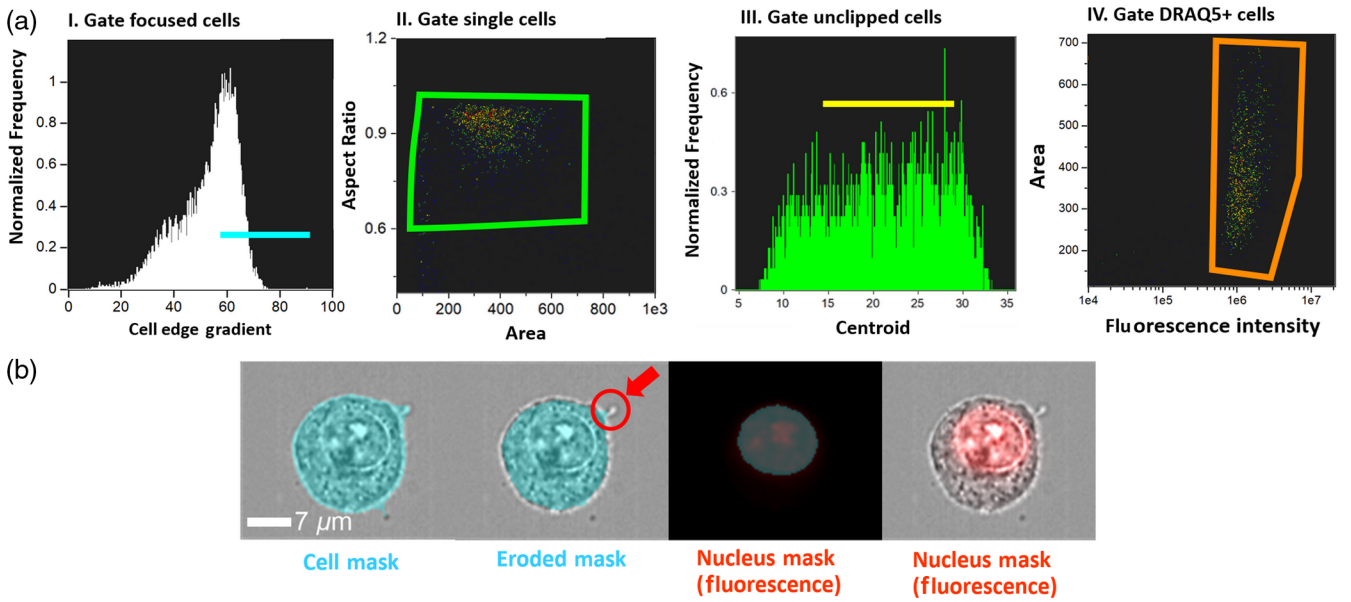


**Fig. 1** (a) An overview of the IFC gating workflow. Sequential gating is applied for excluding: (I) unfocused cells, (II) multiple cells, (III) clipped cells, and (IV) cells, which exhibit no DRAQ-5 signal. Manually gated ROIs are depicted as solid lines in histograms and as ROIs in scatter plots. (b) An example of a representative brightfield cell image as well as the masks used to determine cell and nucleus diameters. An example region of the cell that has been removed by the eroded mask is circled in red. The final panel shows the nucleus mask in red overlaid on the brightfield image.

respectively. All measurements were performed at 37°C. The Petri dishes containing the cells were filled with PBS to provide acoustic coupling and were placed on a translation stage located between the optical objective and the transducer. Cells were located using the optical objective and were translated into the confocal transducer/objective focal zone for measurement. While the location of the features in the power spectrum used for cell and nucleus sizing is robust to the spatial location of the cell within the acoustic detection volume,[34] centering the cell in the focal zone provides optimal signal-to noise ratio (SNR) in the time and frequency domains and increases the prominence of the spectral features.[34] A total of 200 US and 200 PA signals were acquired from each cell for signal averaging. To prevent measurement of the same cell multiple times, the sample was manually translated in a raster pattern until measurements from 50 unique cells had been acquired.

The workflow for the spectral fitting technique used for both the US and the PA RF-lines is provided in Fig. 2. First, a peak detector algorithm was used on the recorded US and PA time-domain signals—the time interval between the two peaks was converted to a distance using the speed of sound to provide a first approximation of the size of the cell and nucleus, respectively. The time-domain signal was then multiplied by a Tukey window and Fourier transformed, with a spectral resolution set to 1 MHz. The US and PA power spectra were then normalized by an appropriate (i.e., US or PA) reference spectrum accordingly to eliminate the system response. As a last step prior to fitting, the power spectra were windowed from 200 to 550 MHz to match the approximate transducer bandwidth and were normalized.

A dictionary containing the theoretical power spectra from 1 MHz to 1 GHz in steps of 1 MHz was generated for spherical absorbers with radii ranging from 0.05 to 50 $\mu$m in steps of 0.05 $\mu$m using the Diebold model for power spectra emitted by a spherical absorber.[35] A speed of sound of 1527 m/s and density of 1000 kg/m$^3$ were used for the background liquid (PBS), and corresponding values of 1560 m/s and 1050 kg/m$^3$ were used for the cells. The estimated cell/nucleus sizes acquired from the time-domain signal were used to constrain the portion of the dictionary used for fitting. For an estimated time-domain radius $a$, the block of power spectra from $a-1$ $\mu$m to $a+1$ $\mu$m was extracted and gated from 200 to 550 MHz to match the measured power spectra. Finally, an inner product was performed between the measured power spectrum and each theoretical spectrum in the extracted dictionary block. The maximum value for the product corresponded to the radius in the dictionary, which provided the best fit to the measured spectra. Owing to the factor of two difference in the argument for US backscatter from cell-like liquid droplets and PA emissions from spherical droplets,[32] the same dictionary could be used for both US and PA fittings—the final values only needing to be scaled by a factor of 0.5 for the US measurements (i.e., the power spectra for a spherical PA source of 10-$\mu$m radius is equivalent to that of the US backscattered power spectra from a liquid droplet with a radius of 5 $\mu$m).

## 3 Results

### 3.1 *Image Flow Cytometer*

For this study, we investigated two different breast cancer cell lines (MCF-7 and MDA-MB-231), as well as PC-3 prostate cancer cells. To determine a baseline for the distribution of cell and nucleus sizes for each cell line, a total of 14,377 MCF-7 cells, 33,678 PC-3 cells, and 18,862 MDA cells were imaged using the IFC. For each cell line, 85% of the acquired images were discarded in the gating process due to the presence of alignment beads, multiple cells or cell fragments in the field of view, or cells that were out of focus in the images. Examples of rejected cell images are shown in Appendix A (Sec. 6). In a

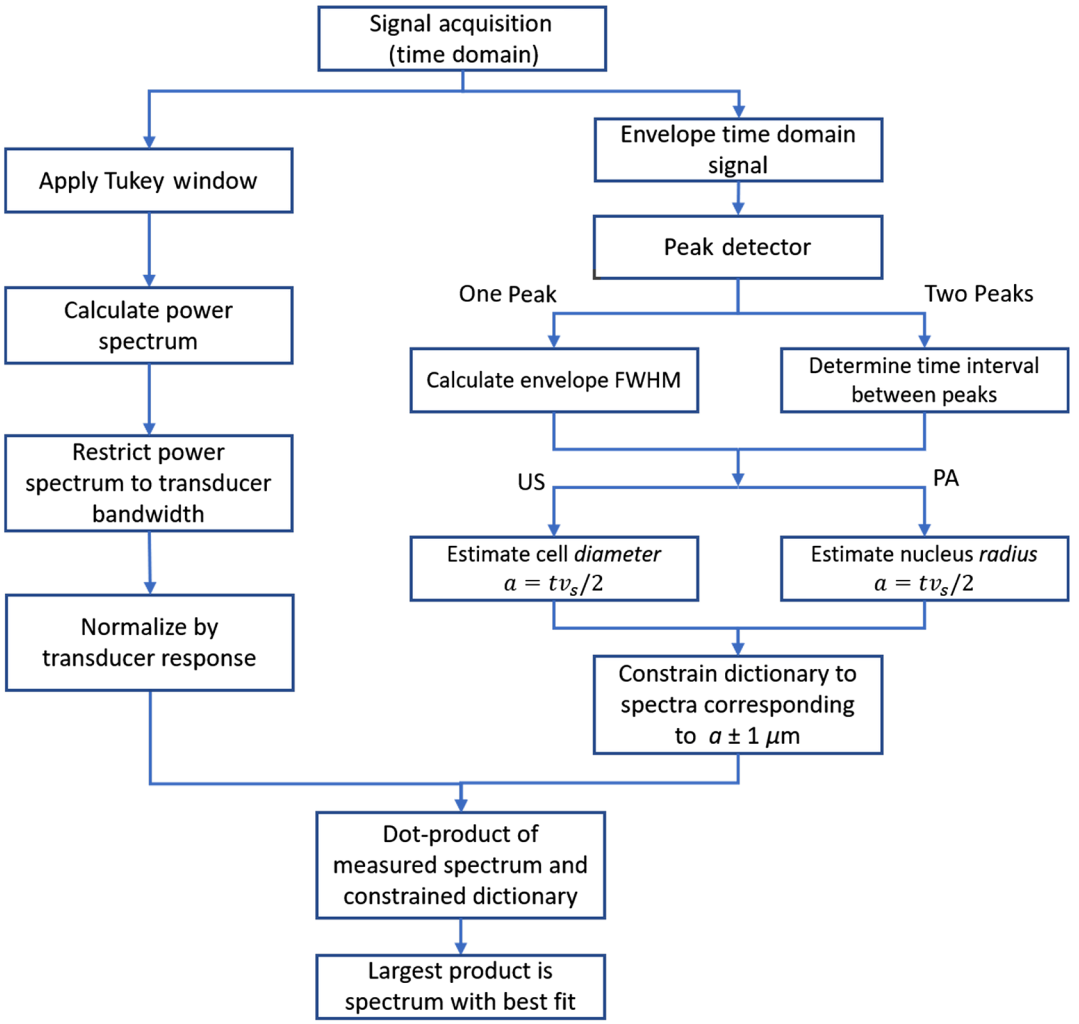


**Fig. 2** The signal processing workflow used for determining the cell and nucleus sizes from the US and PA signals, respectively.

small percentage of cells, the size of the nucleus mask was greater than the size of the cell mask; these images were further excluded from the final datasets. The above exclusion process ensured highly curated datasets consisting of 2164 MCF-7 cells, 4824 PC-3 cells, and 2981 MDA cells, which were then used to determine cell and nucleus size distributions for each cell line using IFC.

A summary of the results of the IFC image analysis for each cell line is provided in Table 1. Comparing the mean equivalent spherical diameters, the MCF-7 cells were the largest ($18.88 \pm 2.86\ \mu$m), followed by the PC-3 ($18.24 \pm 2.22\ \mu$m), and finally the MDA ($16.93 \pm 2.34\ \mu$m). The nuclei of the various cell lines followed a similar trend, with the equivalent spherical nuclear diameter of the MCF-7 cells ($12.68 \pm 1.94\ \mu$m) comparable with the diameter of the PC-3 nuclei ($12.20 \pm 1.86\ \mu$m); however, the size of the average MDA cell nucleus was smaller than the other two cell lines at $11.51 \pm 1.83\ \mu$m. Histograms of the cell and nucleus size distributions for each of the cell lines are provided in Figs. 3(a)–3(c). For each cell in each of the cell line datasets, an N:C ratio was then calculated using the ratio of the cell's equivalent spherical nucleus diameter to the equivalent spherical diameter. The resultant mean N:C ratios for the MCF-7, PC-3, and MDA lines were $0.68 \pm 0.08$, $0.67 \pm 0.07$, and $0.68 \pm 0.08$, respectively.

**Table 1** A summary of the SASAM and image flow cytometer measurements for each cell line.

| | MCF-7 | | PC-3 | | MDA | |
|---|---|---|---|---|---|---|
| Cell line | SASAM ($n = 37$) | IFC ($n = 2004$) | SASAM ($n = 43$) | IFC ($n = 4651$) | SASAM ($n = 43$) | IFC ($n = 2723$) |
| Cell diameter ($\mu$m) | $15.2 \pm 3.5$ | $18.88 \pm 2.86$ | $15.4 \pm 2.9$ | $18.24 \pm 2.22$ | $14.2 \pm 3.0$ | $16.93 \pm 2.34$ |
| Nucleus diameter ($\mu$m) | $10.2 \pm 3.5$ | $12.68 \pm 1.94$ | $10.2 \pm 3.6$ | $12.20 \pm 1.86$ | $7.2 \pm 2.9$ | $11.51 \pm 1.83$ |
| N:C | $0.68 \pm 0.19$ | $0.68 \pm 0.08$ | $0.66 \pm 0.19$ | $0.67 \pm 0.07$ | $0.54 \pm 0.19$ | $0.68 \pm 0.08$ |

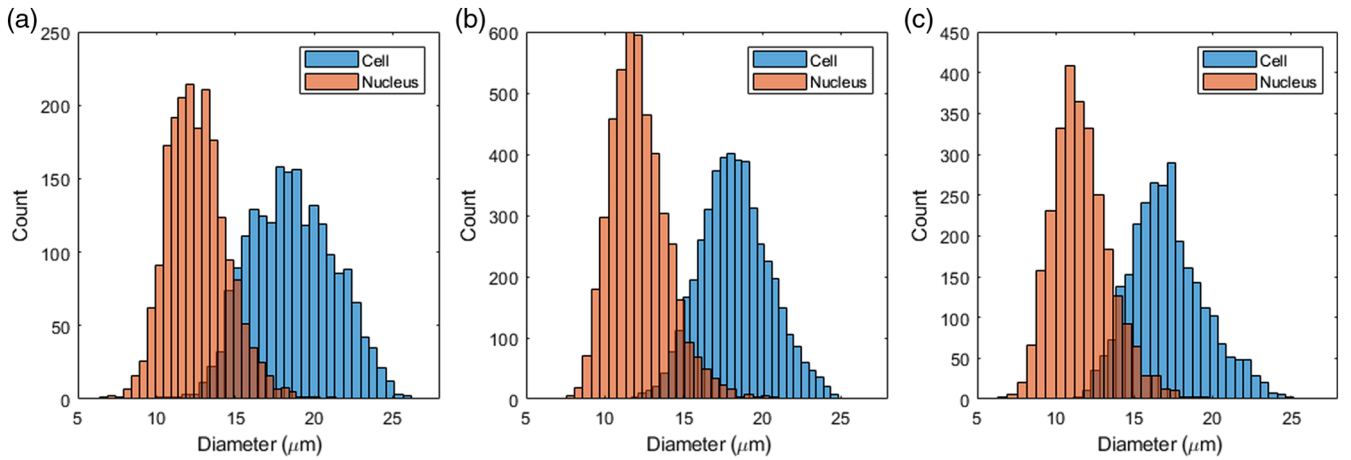


**Fig. 3** Histograms generated from the IFC measurements depicting the distribution of cell and nucleus sizes for the (a) MCF-7 cells, (b) PC-3 cells, and (c) MDA cells.

Representative merged IFC brightfield and fluorescence images of cells with N:C ratios ranging from 0.1 to 0.9 are shown in Fig. 4.

### 3.2 *SASAM Cell Analysis*

Sequential UHF US and PA measurements were performed on 50 unique cells for each cell line. Representative measured US and PA signals from the same cell are shown in Figs. 5(a) and 5(b), respectively. The envelope of each time-domain signal was observed to have either one or two peaks depending on the size of the cell or nucleus being measured. When two peaks are observed, the distance corresponding to the time between the two maxima in the signal envelope provides a rough approximation of the cell or nucleus size and can be used as a constraint in the dictionary fitting algorithm. When only one peak is present in the time-domain signal, the full width at half maximum (FWHM) of the envelope is instead used as an indication of scatterer/absorber size. Since the temporal length of the signals from the cell were longer than that of the PA signals from the nucleus, two well-defined peaks were more commonly observed in the US measurements compared to the PA

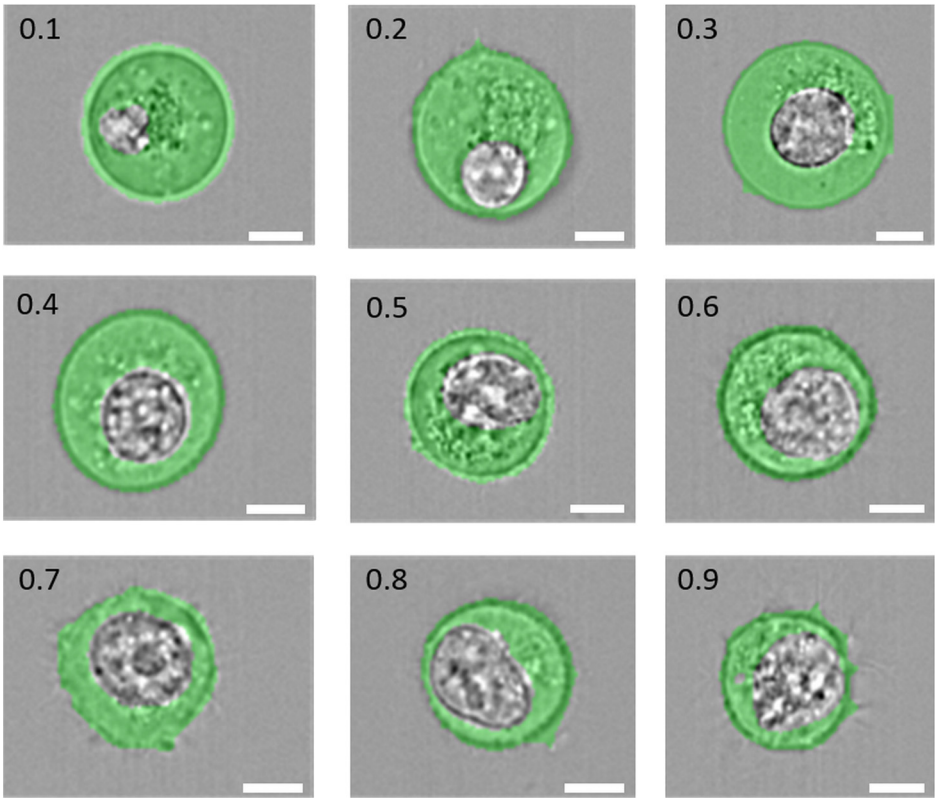


**Fig. 4** Examples of cells having N:C ratios ranging from 0.1 to 0.9, as indicated in the top left corner of each image. The cell cytoplasm has been pseudocolored green, and the nucleus is shown in grayscale. The scale bar in each image is 7 $\mu$m.

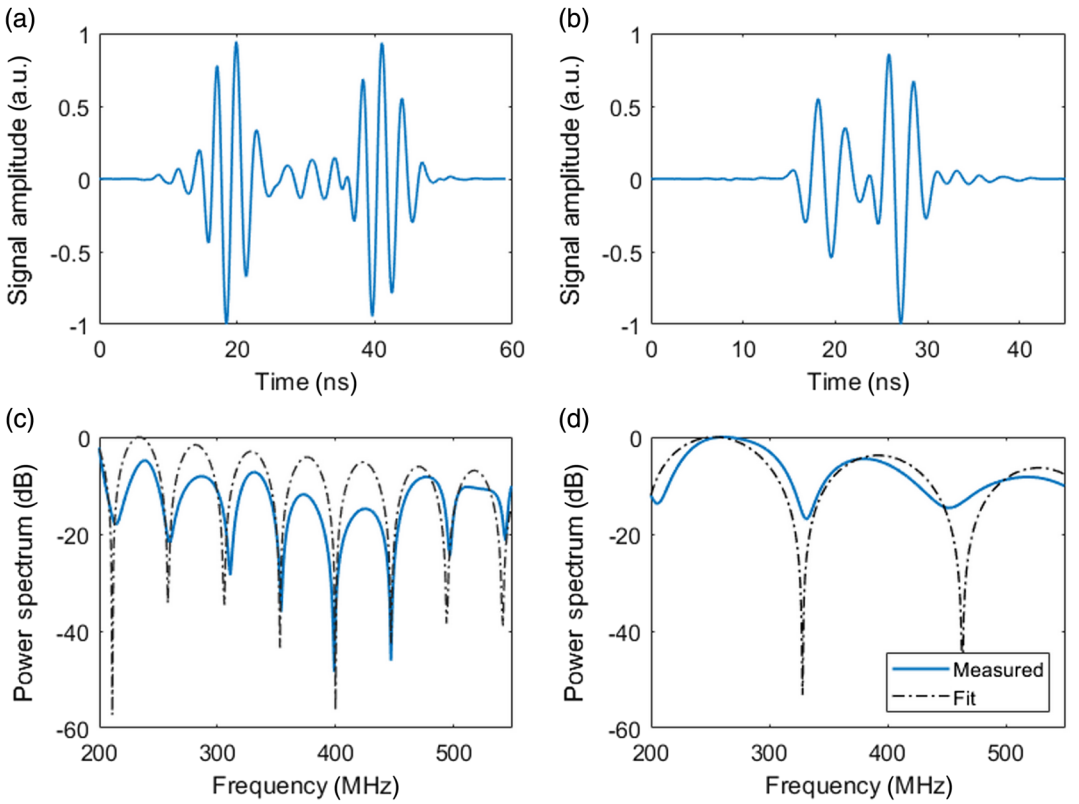


**Fig. 5** Representative (a) US and (b) PA signals from the same MDA-MB-231 cell. The corresponding power spectra are shown in (c) and (d), along with the best-fit power spectrum from the dictionary.

measurements. While a majority of the US/PA measurement pairs were found to have good agreement with at least one of the prepopulated signals in the dictionary, in cases where the fits for either the US or PA measured signal were clearly erroneous for either the US or the PA measurement, both US and PA data points were omitted from the final population statistics. Common reasons for exclusion were: the SNR of either the US or PA signal was inadequate for visualizing spectral features, erroneous fitting results (e.g., where the calculated nucleus size was greater than the cell size), and cells for which the power spectra corresponding to the cell or nucleus sizes predicted by the fitting method were in clear disagreement with the measured spectra. Representative examples of excluded signals are shown in Appendix B (Sec. 7). The total number of cells for which both the US and the PA signals were adequately fit was 37 for the MCF-7 cells, 43 for the PC-3 cells, and 43 for the MDA cells. A summary of the derived values is provided in Table 1. For the MCF-7 line, the measured cells ranged from 8 to 28 $\mu$m in diameter, as determined from the US signals, and the mean cell diameter was calculated to be $15.2 \pm 3.5$ $\mu$m. In contrast, the diameters of the PC-3 cells were more tightly distributed, with diameters ranging from 10 to 22 $\mu$m, and a mean diameter of $15.4 \pm 2.9$ $\mu$m. The MDA cells also had a size distribution from about 8 to 21 $\mu$m in diameter but were the smallest cells on average with a mean diameter of $14.2 \pm 3.0$ $\mu$m. The size of the MCF-7 nuclei, as determined by the PA signals, ranged from 5 to 20 $\mu$m in diameter with a mean diameter of $10.2 \pm 3.5$ $\mu$m. The size of both the PC-3 and MDA cell nuclei ranged from ~4 to 20 $\mu$m in diameter and had mean diameters of $10.2 \pm 3.6$ and $7.2 \pm 2.9$ $\mu$m, respectively. Using the measured values for the cell and nucleus diameters, the N:C ratio was calculated on a cell-by-cell basis for each cell line. The mean N:C ratios were $0.68 \pm 0.19$, $0.66 \pm 0.19$, and $0.54 \pm 0.19$ for the MCF-7, PC-3, and MDA cells, respectively. Box-and-whisker plots showing the resultant distribution of N:C ratios are shown in Fig. 6.

A two-sample $t$-test was used to test for similarity between the means of the three cell lines. A statistically significant difference ($p < 0.05$) was observed between the mean diameter of the PC-3 and MDA cells; however, no statistically significant difference was observed when the other combinations of cell types were compared. In contrast, a significant difference ($p < 0.001$) was observed for the means of the nucleus diameter when comparing either the MCF-7 or PC-3 populations with the MDA. Significant differences ($p < 0.01$) were found when comparing the N:C ratios for the MCF-7 and MDA, and the PC-3 and MDA cell populations.

## 4 Discussion

Owing to the widespread use of the N:C ratio in cancer diagnosis, the ability of morphologists to repeatably and reliably determine the ratio in histology has recently been scrutinized.[5,6] Vaickus and Tambouret[6] found that trained morphologists were prone to overestimations of the ratio, especially at lower N:C values. The authors cited the irregularly shaped cytoplasm of the cells in the histological samples as one of the potential reasons for this discrepancy. In contrast, a larger study by Zhang et al.[5] found that trained participants were adept at identifying both high (>0.7) and low (<0.3) N:C ratios but were less accurate at intermediate N:C ratios. Newer techniques, such as those based on quantitative image analysis, have the

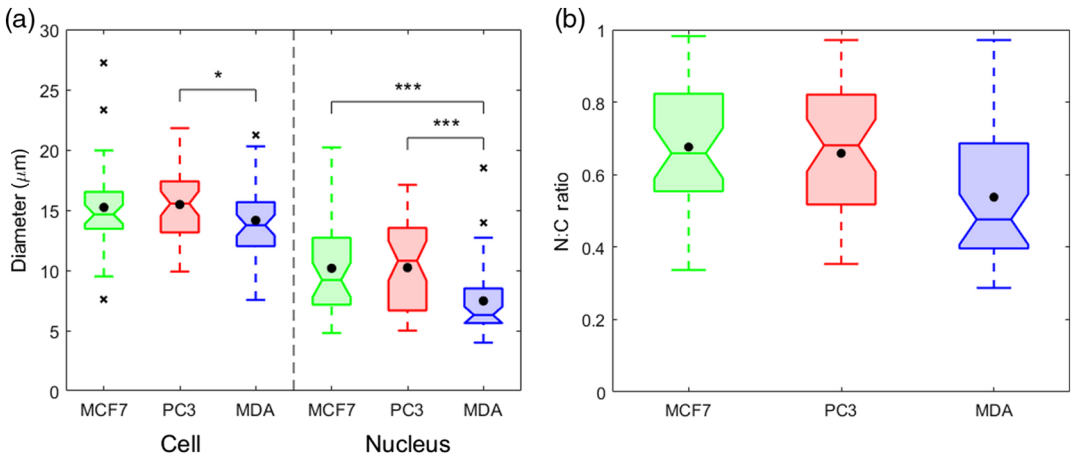


**Fig. 6** (a) Box-and-whisker plots displaying the cell and nucleus sizes determined using the US/PA technique. In each plot, the horizontal colored line indicates the median cell size, and the mean is indicated by the black circle. Outliers are denoted with x. A single asterisk denotes a *p*-value of <0.05, whereas triple asterisks indicate a *p*-value of <0.001. (b) N:C ratios for each cell type.

potential to overcome some of these challenges; however, these techniques are limited to thinly sliced histology samples and cannot be translated to the analysis of emerging diagnostic techniques such as liquid biopsies for circulating tumor cell (CTC) detection.[36]

In this study, an IFC system was used as a means for optically determining the average cell and nucleus diameters for each population of suspended cells. Our intent was for the technique to act as a comparator for the values derived from the US/PA spectral fitting algorithm. While IFC excels at imaging and acquiring 2-D morphology of large cell populations, there are some inherent disadvantages with the technique. The most critical of these is that the IFC is dependent on the masks and features used for gating the population and selecting the images that will be used to generate the statistical results. Care must be taken to ensure that the different masking algorithms used are appropriate for the cell population being analyzed and that the images being analyzed contain no anomalies or artifacts. For example, in the present study, we found that the cell mask used in the IDEAS software tended to incorporate some of the "halo" delineating the edge of the cell cytoplasm, causing the overall cell size to be overestimated by 1 to 2 $\mu$m, if an additional erosion mask was not used. In addition, images had to be excluded from the analysis workflow due to the presence of cellular debris or alignment beads in the image or if the cell was out of focus, off center, or clipped in the field of view. While the final number of cells analyzed was sufficient to generate statistical values with low standard deviation for each cell line, the low percentage (~15%) of usable cell images from the total number of acquired images indicates that rare constituents, such as CTCs, which may be at concentrations as low as 1000 per 10 ml sample volume,[37] could go undetected by current IFC techniques.

To the best of our knowledge, there is currently no method that is accepted as the standard for determining the 3-D morphology of a population of cells and their nuclei while in suspension such as the constituents of liquid biopsies would be. In contrast to conventional N:C assessment methodologies, the dual-modality US/PA technique we present here—which infers the 3-D structure of the cell/nucleus directly from the acquired US and PA signals—is free of user bias and provides quantitative values for the N:C ratio. Furthermore, both the US and the PA interrogation modalities are highly specific to the cell and stained nucleus, respectively. We have previously demonstrated that waveforms of US signals backscattered from individual biological cells are unaffected by cell nuclei since they are acoustically homogeneous at UHFs.[34] Indeed, the presence of a strongly scattering object within the cell would result in either one or two additional peaks in the time-domain signal depending on the size of the nucleus; however, such peaks were not observed in our experiments. While the US measurements are unaffected by the presence of the cell nucleus, the PA measurements are insensitive to the overall size of the cell. This specificity is due to the localization of the dye within the nucleus and the negligible optical absorption of the cytoplasm and other cellular components in the visible spectrum. Thus, the US modality provides only information pertaining to cell morphology, whereas the PA signal contains only information pertaining to the stained nucleus.

Compared to the large number of cells analyzed by the IFC, the cells analyzed using the US/PA technique only provide a snapshot of a small subset of the total cell population. Nevertheless, reasonable agreement was found between the results of both techniques. For all cell lines, the mean cell and nucleus diameters detected using the IFC were larger than those found using the US/PA method. Interestingly, while the maximum cell sizes detected with both techniques were similar, the IFC did not detect any cell <10 $\mu$m in diameter for any of the three cell lines, resulting in a larger mean cell diameter. This could potentially be attributed to the IFC image-masking techniques used being too restrictive and inadvertently removing smaller cells. It is interesting to note that, in both the IFC and the US/PA measurements, all three cell lines had N:C ratios that were slightly <0.70 (i.e., the calculated nucleus diameter for each malignant cell line was ~70% of the total cell diameter). This value is in clear contrast with cells from nonmalignant tissues, which typically have a nucleus that accounts for 45% of the total cell diameter.[38] The only exception to this was the US/PA MDA cell group, which had an N:C ratio of 0.54. However, the large standard deviation due to the small sample size may account for this discrepancy.

Our ultimate goal is to integrate this algorithm into a device that would be capable of screening a blood sample for the presence of CTCs based on their morphological differences (i.e., cell size, nucleus size, N:C ratio) with normally occurring blood

cells. To this end, we investigated the possibility of differentiating between the three different cancer cell lines using our algorithm. The results of the *t*-tests comparing the cell diameters indicate that while the distributions of the MDA and PC-3 cells were significantly different from one another, there was no statistically significant difference between the distribution of cell diameters in the MCF-7 population when compared to either the PC-3 or MDA populations. Thus, for these cell lines, cell size alone cannot be used as a reliable metric for identification of cell type. Using a device that relied only on the overall cell size, such as filtration or electrical impedance measurement, the three cell lines used in this study would be nearly indistinguishable. However, when the nucleus and N:C ratio are additionally considered, differentiation of the MDA cells from the other two cell lines becomes possible, as the distributions of these parameters for the PC-3 and MCF-7 cell lines were both significantly different ($p < 0.001$ for the nucleus size, and $p < 0.01$ for the N:C ratio), when compared to the MDA line. For the number of cells analyzed here, the ability of the US/PA technique to discriminate between the MCF-7 and the PC-3 cell lines was limited due to high standard deviation of the reported mean values; however, when larger cell populations are analyzed, we believe that this will not greatly affect the technique's ability to detect CTCs in a blood sample. Most leukocytes in the blood are between 8 and 11 $\mu$m in diameter, enabling the detection of CTCs in the blood by size-based techniques (e.g., filtration) alone.[39,40] However, techniques based solely on cell size can misclassify large leukocytes and small CTCs. Consideration of additional metrics such as the nucleus size and N:C ratio could further improve the sensitivity of current size-based techniques.

Our previously reported spectral fitting algorithms required at least two spectral minima to fall within the bandwidth of the 400-MHz transducer[34] and were thus incapable of sizing spherical cells or organelles with diameter smaller than ~3.5 $\mu$m when using US, or 7 $\mu$m when using PA. These limitations are acceptable when using US to determine cell size since most animal cells typically have diameters between 10 and 20 $\mu$m.[38] However, as the IFC measurements revealed, in some cases, cell nuclei can be as small as 4.5 $\mu$m in diameter and so our previous algorithm would be insufficient for determining the size of small nuclei from their emitted PA signals. The inner product spectral fitting technique presented here is advantageous in that it uses the entire frequency-domain spectrum within the transducer bandwidth to deduce the size of the absorber. Thus, cells and nuclei that are smaller than the above limits and have fewer than two spectral features can readily be sized. Another advantage of the present algorithm is that the equations governing the shape of the power spectrum for spherical cells and nuclei with acoustic properties similar to their surroundings differ only by a factor of 2 in the argument.[32] This means that the same dictionary can be used to determine the size of both cells and nuclei, reducing the computational time and complexity of the algorithm. One limiting factor of the current technique is that the theory used for predicting absorber size from the PA power spectra is only valid for spherical absorbers. Thus, nuclei with high aspect ratios would not be able to be fit using the current technique. Going forward, we plan to incorporate analytical models capable of accurately determining the morphology and orientation of nonspherical nuclei, such as those shaped like prolate and oblate spheroids.[41,42] Incorporating models such as these would increase the robustness and accuracy of the present technique and potentially eliminate some of the disagreements observed in some of the discarded power spectrum fits.

## 5 Conclusion

In this work, we sought to validate the cell, nucleus, and N:C ratio values obtained using our sound-based technique with population values obtained using the optical IFC device. We demonstrate that, while there were slight differences in the overall size of the cells predicted by the two techniques, good agreement between the two techniques was observed, especially for the calculated N:C ratio values. We have recently reported on an acoustic flow cytometer that sized cell diameter using only US methods[34] and have since incorporated a pulsed laser into our system to enable differentiation of RBCs and white blood cells via simultaneous US/PA detection.[43] Going forward, we plan on translating the presently reported N:C assessment technique to this high-throughput US/PA device to enable large-scale investigations of cell population statistics, as well as the detection of cancer cells spiked into a blood sample.

## 6 Appendix A: Examples of Rejected Imaging Flow Cytometer Cell Images, as Well as Reasons for Rejection

Examples of cells that were excluded from the IFC analysis by means of gating are shown in Fig. 7. In Fig. 7(a), the imaged cell is out of focus, resulting in a large "halo" at the cell periphery, which would lead to an overestimation of the cell diameter.

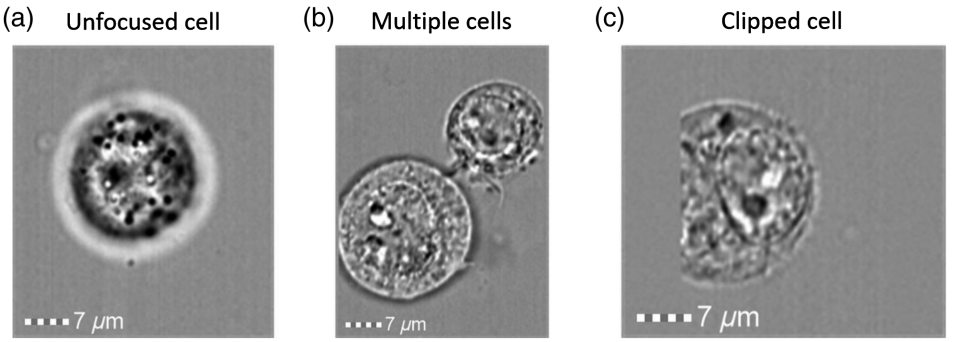


**Fig. 7** (a) An example of an out-of-focus cell exhibiting a large intensity gradient at the cell periphery. (b) A rejected IFC image containing multiple cells. (c) An IFC image depicting a cell that has had its left side clipped from the ROI.

Figure 7(b) depicts an image that was rejected on the grounds that two cells were detected in the ROI. Finally, Fig. 7(c) shows an image of a cell which was "clipped" at the edge of the image ROI, and thus unsuitable for analysis.

## 7 Appendix B: Examples of Rejected Ultrasound/Photoacoustic Cell Measurements

The graphs in Fig. 8 provide examples of RF-lines and power spectra which were excluded from analysis. In Fig. 8(a) the acquired PA waveform has poor SNR, causing an estimation of nucleus size from the PA power spectrum [Fig. 8(b), right] that is larger than the fit cell diameter [Fig. 8(b), left]. Conversely, in Fig. 8(c) there is increased noise in the acquired US RF-line, leading to a poor fit in the US power spectrum [Fig. 8(d), left] and an under-estimation of cell size.

### *Disclosures*

M.C.K. and M.J.M. have financial interests in Echofos Medical Inc., which, however, did not support this work. The remaining author declares no competing financial interests.


### *Acknowledgments*

We would like to thank Eric Strohm for many fruitful conversations, Michael Parsons for his assistance with the ImageStream Flow Cytometer, as well as Celina Yang and Aren Gharabeiki for their assistance in culturing some of the cell lines used in this experiment. This research was supported in part by the Natural Sciences and Engineering Research Council of Canada, the Canadian Cancer Society, the Canadian Foundation for Innovation, the Ontario Ministry for Research and Innovation, and the Terry Fox Foundation Funding agencies.


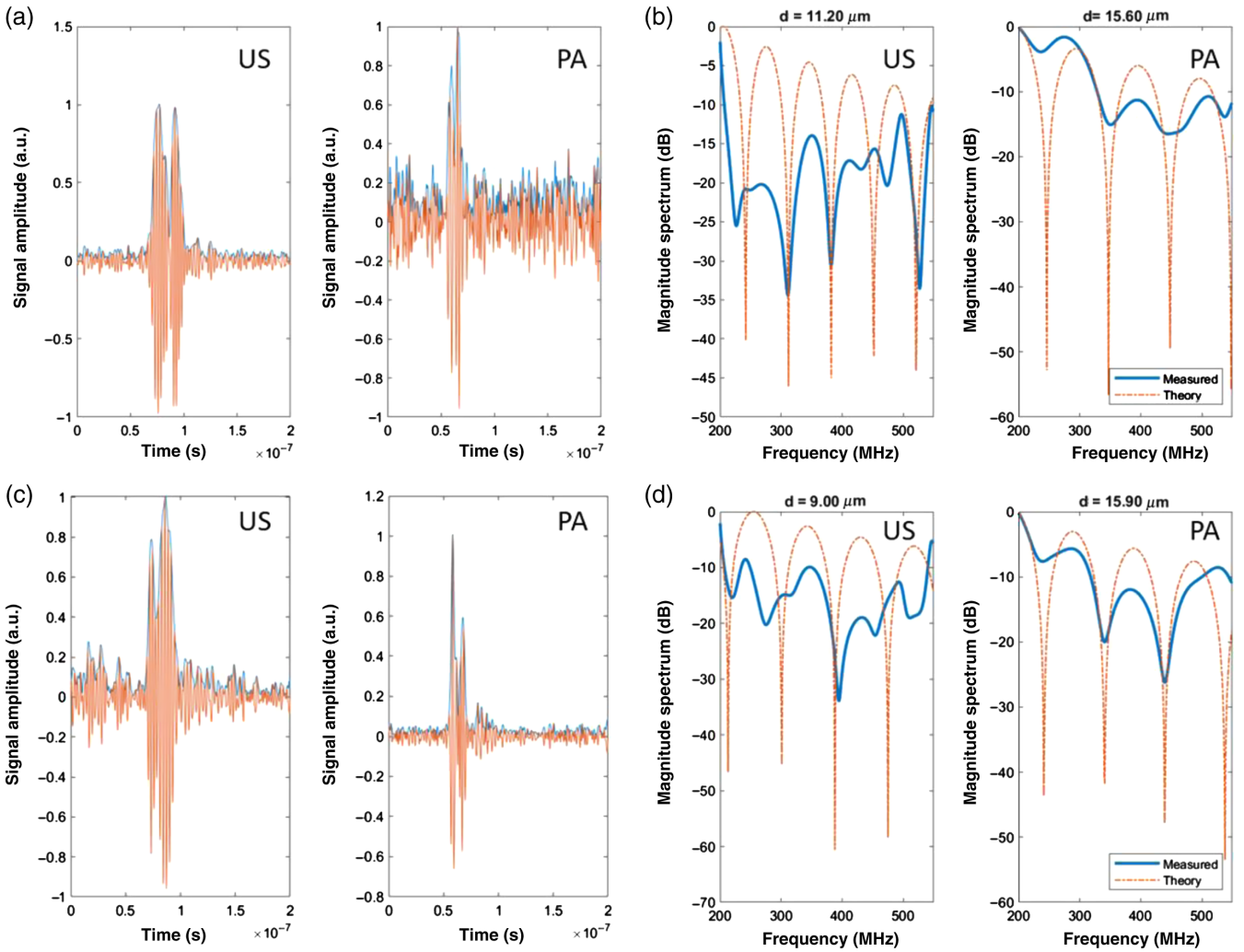


**Fig. 8** For the power spectra, the fit diameter is indicated above the graph axis. In (a), the noisy PA signal resulted in a power spectrum (b) with minima placement indicative of a nucleus size larger than that of the cell size. In (c), a noisy US spectrum resulted in a poor fit to the theoretical US backscatter, causing (d) the cell size to be underestimated.

## References


1. C. Fletcher, *Diagnostic Histopathology of Tumors*, 4 ed., Elsevier/Saunders, Philadelphia (2013).
2. H. Hillman, "Limitations of clinical and biological histology," *Med. Hypotheses* **54**(4), 553–564 (2000).
3. C. Su Lim et al., "Measurement of the nucleus area and nucleus/cytoplasm and mitochondria/nucleus ratios in human colon tissues by dual-colour two-photon microscopy imaging," *Sci. Rep.* **5**, 1–11 (2015).
4. L. J. Layfield et al., "Accuracy and reproducibility of nuclear/cytoplasmic ratio assessments in urinary cytology specimens," *Diagn. Cytopathol.* **45**(2), 107–112 (2017).
5. M. L. Zhang, A. X. Guo, and C. J. VandenBussche, "Morphologists overestimate the nuclear-to-cytoplasmic ratio," *Cancer Cytopathol.* **124**(9), 669–677 (2016).
6. L. J. Vaickus and R. H. Tambouret, "Young investigator challenge: the accuracy of the nuclear-to-cytoplasmic ratio estimation among trained morphologists," *Cancer Cytopathol.* **123**(9), 524–530 (2015).
7. P. J. McIntire et al., "Digital image analysis supports a nuclear-to-cytoplasmic ratio cutoff value below 0.7 for positive for high-grade urothelial carcinoma and suspicious for high-grade urothelial carcinoma in urine cytology specimens," *Cancer Cytopathol.* **127**(2), 120–124 (2019).
8. A. Z. Khan et al., "Nucleus morphometry in cultured epithelial cells correlates with phenotype," *Microsc. Microanal.* **22**(3), 612–620 (2016).
9. H.-C. Huang et al., "Comparison of two- and three-dimensional nuclear to cytoplasm ratios in analyzing lung cancer cell lines," *Proc. SPIE* **10881**, 108810V (2019).
10. P. Balasubramanian et al., "Confocal images of circulating tumor cells obtained using a methodology and technology that removes normal cells," *Mol. Pharm.* **6**(5), 1402–1408 (2009).
11. E. K. Zuba-Surma and M. Z. Ratajczak, "Analytical capabilities of the ImageStream cytometer," *Methods Cell Biol.* **102**, 207–230 (2011).
12. V. Nandakumar et al., "Isotropic 3D nuclear morphometry of normal, fibrocystic and malignant breast epithelial cells reveals new structural alterations," *PLoS One* **7**(1), e29230 (2012).
13. V. Nandakumar et al., "Quantitative characterization of preneoplastic progression using single-cell computed tomography and three-dimensional karyometry," *Cytom. Part A* **79 A**(1), 25–34 (2011).
14. R. N. Pinto et al., "Label-free analysis of red blood cell storage lesions using imaging flow cytometry," *Cytom. Part A* **95**(9), 976–984 (2019).
15. R. N. Pinto et al., "Application of image flow cytometry for the characterization of red blood cell morphology," *Proc. SPIE* **10076**, 100761F (2017).
16. Amnis Corporation, "IDEAS® Image data exploration and analysis software user's manual," Version 4.0, Washington (2010).
17. K. E. McGrath, T. P. Bushnell, and J. Palis, "Multispectral imaging of hematopoietic cells: where flow meets morphology," *J. Immunol. Methods* **336**(2), 91–97 (2008).
18. K. E. McGrath, "Utilization of imaging flow cytometry to define intermediates of megakaryopoiesis in vivo and in vitro," *J. Immunol. Methods* **423**, 45–51 (2015).
19. S. Bekeschus et al., "High throughput image cytometry micronucleus assay to investigate the presence or absence of mutagenic effects of cold physical plasma," *Environ. Mol. Mutagen.* **59**(4), 268–277 (2018).
20. I. A. Vorobjev et al., "Imaging flow cytometry analysis of intracellular pathogens," *Methods* **112**, 91–104 (2016).
21. E. Hysi, E. M. Strohm, and M. C. Kolios, "Probing different biological length scales using photoacoustics: from 1 to 1000 MHz," in *Handbook of Photonics for Biomedical Engineering*, A. P. Ho, D. Kim, and M. Somekh, Eds., pp. 303–324, Springer, Dordrecht (2017).
22. L. V. Wang and S. Hu, "Photoacoustic tomography: in vivo imaging from organelles to organs," *Science* **335**(6075), 1458–1462 (2012).
23. S. Gottschalk et al., "Rapid volumetric mapping of neural dynamics across the mouse brain by optoacoustic calcium imaging," *Nat. Biomed. Eng.* **3**, 392–401 (2019).
24. J. Shi et al., "High-resolution, high-contrast mid-infrared imaging of fresh biological samples with ultraviolet-localized photoacoustic microscopy," *Nat. Photonics* **13**, 609–615 (2019).
25. M. Omar, J. Aguirre, and V. Ntziachristos, "Optoacoustic mesoscopy for biomedicine," *Nat. Biomed. Eng.* **3**, 354–370 (2019).
26. M. J. Moore et al., "Photoacoustic F-mode imaging for scale specific contrast in biological systems," *Commun. Phys.* **2**, 30 (2019).
27. E. M. Strohm and M. C. Kolios, "Classification of blood cells and tumor cells using label-free ultrasound and photoacoustics," *Cytom. Part A* **87**(8), 741–749 (2015).
28. E. M. Strohm, M. J. Moore, and M. C. Kolios, "Single cell photoacoustic microscopy: a review," *IEEE J. Sel. Top. Quantum Electron.* **22**(3), 137–151 (2016).
29. E. M. Strohm, E. S. L. Berndl, and M. C. Kolios, "Probing red blood cell morphology using high-frequency photoacoustics," *Biophys. J.* **105**(1), 59–67 (2013).
30. V. C. Anderson, "Sound scattering from a fluid sphere," *J. Acoust. Soc. Am.* **22**, 426–431 (1950).
31. H. G. Frey and R. R. Goodman, "Acoustic scattering from fluid spheres," *J. Acoust. Soc. Am.* **40**(2), 417–420 (1966).
32. M. J. Moore, E. M. Strohm, and M. C. Kolios, "Assessment of the nucleus-to-cytoplasmic ratio in MCF-7 cells using ultra-high frequency ultrasound and photoacoustics," *Int. J. Thermophys.* **37**(12), 118 (2016).
33. J. A. Sebastian, M. J. Moore, and M. C. Kolios, "Comparison of measurements of the nucleus-to-cytoplasmic ratio in MCF-7 cells using ultra-high frequency photoacoustic microscopy and imaging flow cytometry," *Proc. SPIE* **10878**, 108784M (2019).
34. E. M. Strohm et al., "Sizing biological cells using a microfluidic acoustic flow cytometer," *Sci. Rep.* **9**(4775), 1–10 (2019).
35. G. J. Diebold and P. J. Westervelt, "The photoacoustic effect generated by a spherical droplet in a fluid," *J. Acoust. Soc. Am.* **84**(6), 2245–2251 (1988).
36. C. Alix-Panabières and K. Pantel, "Circulating tumor cells: liquid biopsy of cancer," *Clin. Chem.* **59**(1), 110–118 (2013).
37. S. Nagrath et al., "Isolation of rare circulating tumour cells in cancer patients by microchip technology," *Nature* **450**, 1235–1239 (2007).
38. B. Alberts et al., *Molecular Biology of the Cell*, 6th ed., Garland Science, Taylor & Francis Group, LLC., New York (2015).
39. P. Paterlini-Brechot and N. L. Benali, "Circulating tumor cells (CTC) detection: clinical impact and future directions," *Cancer Lett.* **253**(2), 180–204 (2007).
40. S. Meng et al., "Circulating tumor cells in patients with breast cancer dormancy," *Clin Cancer Res.* **10**, 8152–8162 (2004).
41. Y. Li et al., "Simulating photoacoustic waves produced by individual biological particles with spheroidal wave functions," *Sci. Rep.* **5**, 14801 (2015).
42. Y. Li et al., "Analytic theory of photoacoustic wave generation from a spheroidal droplet," *Opt. Express* **22**(17), 19953 (2014).
43. V. Gnyawali et al., "Simultaneous acoustic and photoacoustic microfluidic flow cytometry for label-free analysis," *Sci. Rep.* **9**, 1585 (2019).



**Michael J. Moore** received his BMath degree in mathematical physics from the University of Waterloo, Ontario, Canada, in 2013, and his PhD in biomedical physics at Ryerson University, Ontario, Canada, in 2018. Currently, he is employed as a medical physics resident at Grand River Regional Cancer Centre in Kitchener, Ontario, Canada. His research interests include acoustic microscopy, photoacoustic (PA) microscopy, and high-frequency quantitative PA of single biological cells.

**Joseph A. Sebastian** received his BEng degree in biomedical engineering from Ryerson University, Ontario, Canada, in 2019. Currently, he is a PhD student at the University of Toronto in the Institute for Biomaterials and Biomedical Engineering. His research interests include high-frequency quantitative ultrasound (US) and PA, flow cytometry, and tissue engineering.

**Michael C. Kolios** is a professor in the Department of Physics at Ryerson University and associate dean of Research and Graduate Studies in the Faculty of Science. His work focuses on the use of US and optics in the biomedical sciences. He has received numerous awards, including the Canada Research Chair in Biomedical Applications of Ultrasound, the Ontario Premiers Research Excellence Award, and in 2016 he received the AIUM Joseph H. Holmes Basic Science Pioneer Award.